The Astrophysical Journal, 943:50 (9pp), 2023 January 20 https://doi.org/10.3847/1538-4357/acaaf9

NOEMA Detection of Circumnuclear Molecular Gas in X-Ray Weak Dual Active Galactic Nuclei: No Evidence for Heavy Obscuration

Meicun Hou[1], Zhiyuan Li[2,3], Xin Liu[4,5], Zongnan Li[6], Ruancun Li[1,7], Ran Wang[1,7], Jing Wang[1], and Luis C. Ho[1,7]
[1] Kavli Institute for Astronomy and Astrophysics, Peking University, Beijing 100871, People's Republic of China; houmc@pku.edu.cn
[2] School of Astronomy and Space Science, Nanjing University, Nanjing 210023, People's Republic of China
[3] Key Laboratory of Modern Astronomy and Astrophysics (Nanjing University), Ministry of Education, Nanjing 210023, People's Republic of China
[4] Department of Astronomy, University of Illinois at Urbana-Champaign, Urbana, IL 61801, USA
[5] National Center for Supercomputing Applications, University of Illinois at Urbana-Champaign, 605 East Springfield Avenue, Champaign, IL 61820, USA
[6] National Astronomical Observatories, Chinese Academy of Sciences, 20A Datun Road, Chaoyang District, Beijing, People's Republic of China
[7] Department of Astronomy, School of Physics, Peking University, Beijing 100871, People's Republic of China
Received 2022 September 27; revised 2022 November 23; accepted 2022 December 11; published 2023 January 24

Abstract

Dual active galactic nuclei (AGNs), which are the manifestation of two actively accreting supermassive black holes (SMBHs) hosted by a pair of merging galaxies, are a unique laboratory for studying the physics of SMBH feeding and feedback during an indispensable stage of galaxy evolution. In this work, we present NOEMA CO(2–1) observations of seven kiloparsec-scale dual-AGN candidates drawn from a recent Chandra survey of low redshift, optically classified AGN pairs. These systems are selected because they show unexpectedly low 2–10 keV X-ray luminosities for their small physical separations signifying an intermediate-to-late stage of merger. Circumnuclear molecular gas traced by the CO(2–1) emission is significantly detected in six of the seven pairs and 10 of the 14 nuclei, with an estimated mass ranging between $(0.2–21) \times 10^9\,M_\odot$. The primary nuclei, i.e., the ones with the higher stellar velocity dispersion, tend to have a higher molecular gas mass than the secondary. Most CO-detected nuclei show a compact morphology, with a velocity field consistent with a kiloparsec-scale rotating structure. The inferred hydrogen column densities range between 5×10^{21}–$2 \times 10^{23}\,\mathrm{cm}^{-2}$, but mostly at a few times $10^{22}\,\mathrm{cm}^{-2}$, in broad agreement with those derived from X-ray spectral analysis. Together with the relatively weak mid-infrared emission, the moderate column density argues against the prevalence of heavily obscured, intrinsically luminous AGNs in these seven systems, but favors a feedback scenario in which AGN activity triggered by a recent pericentric passage of the galaxy pair can expel circumnuclear gas and suppress further SMBH accretion.

Unified Astronomy Thesaurus concepts: Active galaxies (17); Interacting galaxies (802); Active galactic nuclei (16); Submillimeter astronomy (1647); Interferometry (808); CO line emission (262); Galaxy mergers (608)

1. Introduction

Galaxy mergers, during which two galaxies exert strong gravitational force on each other and reshape the structure of their stellar and gaseous content, have long been recognized as a fundamental process in galaxy evolution (Toomre & Toomre 1972; Barnes & Hernquist 1992). In particular, mergers tend to drive a gas inflow toward the center of either galaxy, or both, potentially triggering nuclear star formation (Olson & Kwan 1990; Barton et al. 2000; Nikolic et al. 2004; Kewley et al. 2006). In the meantime, a central supermassive black hole (SMBH), if it exists, can be fed by the same gas inflow and become an active galactic nucleus (AGN; Kauffmann & Haehnelt 2000; Di Matteo et al. 2005; Goulding et al. 2018). In principle, a galaxy merger can trigger a pair of AGNs, i.e., two simultaneously actively accreting SMBHs, also conventionally referred to as "dual AGNs" for pairs with a projected separation $r_p \lesssim 10$ kpc. Dual AGNs are valuable laboratories not only because they provide a crucial observational test for the theory and numerical simulations of galaxy mergers, but also because they are unique targets for studying the rich astrophysics involved in the feeding and feedback of SMBHs during an indispensable stage of galaxy evolution (see the recent review by De Rosa et al. 2019).

Over the past decade, a number of systematic searches for dual-AGN candidates have been conducted, primarily in the optical band thanks to wide-field spectroscopic surveys such as the Sloan Digital Sky Survey (SDSS). In particular, the search for galactic nuclei with double-peaked narrow emission lines (e.g., [O III]λ5007; Comerford et al. 2009; Liu et al. 2010; Smith et al. 2010; Ge et al. 2012; Lyu & Liu 2016) aims at tight AGN pairs (typically 1–10 kpc in separation, but even less) that pertain to the late stage of mergers, while the search for spatially resolved AGN pairs showing optical emission-line characteristics of Seyferts or low-ionization nuclear emission-line regions (LINERs) covers a wider range of projected separation up to $r_p \approx 100$ kpc (Liu et al. 2011). Confirmation of the AGN nature in these optically selected candidates, however, often requires follow-up observations in the X-ray and/or radio bands (Comerford et al. 2011; Teng et al. 2012; Liu et al. 2013; Gabanyi et al. 2016; Brightman et al. 2018; De Rosa et al. 2018; Hou et al. 2019; Peng et al. 2022), which are generally thought to trace immediate radiation from the SMBH and tend to be more immune to obscuration by circumnuclear cold gas. Infrared observations have also played an effective role in revealing dual AGNs, especially in gas-rich merging systems (Satyapal et al. 2014, 2017; Ellison et al. 2017; Weston et al. 2017). Alternatively, one starts with a hard ($\gtrsim$few keV)

X-ray selected AGN and tries to associate it with another AGN in a companion galaxy, if present (Koss et al. 2012). Or, one tries to identify dual AGNs directly from high-resolution radio images (Fu et al. 2015a, 2015b). These approaches have achieved varied degrees of success, revealing a growing number of dual AGNs at low redshift ($z \lesssim 0.5$).

Despite the continued observational effort, a consensus on the occupation rate of AGNs in mergers, and more generally in interacting galaxies, is still absent. This is tied to the challenge of detecting low-luminosity AGNs (i.e., bolometric luminosity $L_{\rm bol} \lesssim 10^{43}$ erg s^{-1}), which are the manifestation of SMBHs fed at relatively low rates. Because less fuel is required, secular processes such as instabilities driven by bars and/or minor mergers, may be sufficient to trigger low-luminosity AGNs (Ho 2008, 2009; Hopkins et al. 2014; Menci et al. 2014). This leaves the causality between galaxy interactions and AGN triggering an open question. Indeed, some observations found an excess of close neighbors in AGN host galaxies or a higher fraction of AGNs in interacting galaxies than in isolated galaxies (Koss et al. 2010; Ellison et al. 2011; Silverman et al. 2011; Liu et al. 2012; Goulding et al. 2018), whereas others detected no significant difference (Ellison et al. 2008; Darg et al. 2010; Villforth et al. 2014, 2017).

Recently, Hou et al. (2020) presented the first systematic X-ray study of optically selected AGN pairs at low redshift (median redshift $\bar{z} \sim 0.1$), based on a homogeneous sample of $\sim 10^3$ SDSS AGN pairs identified by Liu et al. (2011). Utilizing archival Chandra observations, Hou et al. (2020) were able to detect or place significant constraint on the nuclear X-ray emission in a subset of 67 pairs, down to a limiting 2–10 keV X-ray luminosity $L_{\rm X} \sim 10^{40}$ erg s^{-1}. Moreover, interesting trends are revealed in the mean AGN X-ray luminosity as a function of projected separation: First, $L_{\rm X}$ increases with decreasing r_p when $r_p \gtrsim 15$ kpc, suggesting enhanced SMBH accretion even at the early stage of mergers. Second, $L_{\rm X}$ decreases with decreasing r_p at $r_p \lesssim 15$ kpc, when $r_p \lesssim 5$ kpc falling to a mean value below that of single AGNs whose host galaxy properties have been matched to the AGN pair sample. The latter trend is particularly surprising and not predicted by existing numerical simulations of galaxy mergers (e.g., Capelo et al. 2015; Capelo & Dotti 2017; Yang et al. 2019). Hou et al. (2020) considered two plausible explanations: (i) At the intermediate-to-late stage of the merger, gas inflows have led to a central concentration of cold gas that heavily obscures even the hard (2–10 keV) X-rays; (ii) AGN feedback triggered by recent pericentric passage of the galaxy pair can expel gas from the central region and suppress subsequent SMBH accretion.

The first scenario can be directly tested by the detection (or nondetection) of circumnuclear molecular gas with an equivalent hydrogen column density as high as 10^{23}–10^{24} cm^{-2}, required to block keV X-rays from the embedded AGN. To shed light on the cause of the apparently low nuclear X-ray luminosities in the merging pairs with the smallest projected separations ($r_p \lesssim 5$ kpc), we have conducted high-resolution CO observations using the IRAM Northern Extended Millimeter Array (NOEMA), aiming to detect circumnuclear molecular gas in a pilot sample drawn from Hou et al. (2020). Most previous studies of molecular gas in interaction galaxies and mergers have focused on gas-rich, (ultra)luminous infrared galaxies (e.g., Evans et al. 2002; Sakamoto et al. 2008, 2014; Feruglio et al. 2015; Sliwa et al. 2017; Herrera-Camus et al. 2020; Tan et al. 2021), with specific interest in studying molecular outflows. There have also been studies of molecular gas in normal interacting galaxies, which focus on the statistical relation between molecular gas and star-forming activities (Kaneko et al. 2013, 2017; Michiyama et al. 2016; Violino et al. 2018; Shangguan et al. 2019; Thorp et al. 2022). Relatively little attention has been paid to the relation between circumnuclear molecular gas and AGN activity in optically (via [O III]) and X-ray selected, kiloparsec-scale mergers such as those studied here.

This paper is organized as follows. Section 2 describes the target selection, NOEMA CO(2–1) observations, and data reduction. The detection of CO(2–1) emission and the inferred properties of circumnuclear molecular gas in the dual AGNs are presented in Section 3. Main conclusions and implications of this study are addressed in Section 4. Throughout this paper, we assume a concordance cosmology with $\Omega_m = 0.3$, $\Omega_\Lambda = 0.7$, and $H_0 = 70$ km s^{-1} Mpc^{-1}. Errors are quoted at 1σ confidence level, unless otherwise stated.

2. Sample Selection and Data Reduction

2.1. Target Selection

Our targets of seven dual AGNs were drawn from the sample of Hou et al. (2020; hereafter H20), which consists of 67 candidate AGN pairs with archival Chandra observations. The H20 sample itself was drawn from a parent sample of 1286 optical spectroscopic AGN pairs selected from SDSS DR7 (Liu et al. 2011), which are dominated by type 2 AGNs whose optical narrow emission-line ratios are characteristic of Seyferts, LINERs, and/or AGN-[H II] composites. All those AGN pairs have projected physical separations $r_{\rm p} < 100$ kpc and line-of-sight velocity offsets < 600 km s^{-1}. Here for the pilot study, we selected the most closely separated dual-AGN candidates, which include seven systems with $r_{\rm p} < 4.5$ kpc. In the X-ray (0.5–8 keV) band, four systems have both nuclei detected and three have one nucleus detected; when only the hard X-ray band (i.e., 2–10 keV) is considered, five of the 14 nuclei are detected. The 2–10 keV X-ray luminosities (or upper limits) of the 14 nuclei range between 4.6×10^{40}–1.9×10^{42} erg s^{-1}, and their mean luminosity is systematically lower than that of the more separated (i.e., $r_{\rm p} \gtrsim 5$ kpc) nuclei in the H20 sample. The basic information of the 14 nuclei as well as their host galaxies are listed in Table 1. We use 'P' ('S') to denote the primary (secondary) nucleus in a pair, which has the higher (lower) stellar velocity dispersion measured from the SDSS single-fiber spectra.[8]

2.2. NOEMA Observations and Data Reduction

We observed the targets with NOEMA between 2020 October and 2021 January using the single-field observing mode under C-configuration (project: S20BJ; PI: M. Hou). A total of 9–11 antennas participated in the observations, depending on the target. The observations aim to probe the circumnuclear molecular gas via the CO(2–1) line at a rest-frame frequency of 230.54 GHz. Compared to CO(1–0), CO(2–1) is more sensitive to the high column densities of molecular gas expected in the dual AGNs and allows for a

[8] While stellar velocity dispersion is provided by the MPA-JHU catalog (https://wwwmpa.mpa-garching.mpg.de/SDSS/DR7/), here we have employed the penalized pixel-fitting (pPXF) algorithm (Cappellari & Emsellem 2004) to fit the SDSS spectra to extract the stellar kinematics. The best-fit stellar line-of-sight velocity and velocity dispersion are in good agreement with the MPA-JHU values in most cases.

Table 1
Basic Information of Seven Dual AGNs

Full Name (1)	Redshift (2)	ΔV (3)	$\Delta\theta$ (4)	r_p (5)	σ_* (6)	log L_{2-10} (7)	log L_X/L_{Edd} (8)	W1 − W2 (9)
J002208.69+002200.5 (S)	0.0710	93	3.1	4.2	199.4 ± 6.4	<40.85 (1)	< −5.36	0.03 ± 0.03
J002208.83+002202.8 (P)	0.0707	93	3.1	4.2	231.2 ± 5.2	<40.91 (1)	< −5.57	0.03 ± 0.03
J085837.53+182221.6 (S)	0.0587	58	2.9	3.3	130.2 ± 10.3	<40.83 (1)	< −4.59	0.26 ± 0.03
J085837.68+182223.4 (P)	0.0589	58	2.9	3.3	186.5 ± 8.0	<40.97 (1)	< −5.11	0.26 ± 0.03
J102700.40+174901.0 (P)	0.0665	28	2.4	3.0	156.2 ± 5.3	<40.67 (0)	< −5.09	0.17 ± 0.05
J102700.56+174900.3 (S)	0.0666	28	2.4	3.0	133.2 ± 7.3	$40.81^{+0.13}_{-0.15}$ (1)	$-4.66^{+0.06}_{-0.15}$	0.17 ± 0.05
J105842.44+314457.6 (S)	0.0728	172	2.9	4.1	108.8 ± 16.6	<41.28 (1)	< −3.81	0.46 ± 0.04
J105842.58+314459.8 (P)	0.0723	172	2.9	4.1	158.8 ± 14.7	$42.29^{+0.05}_{-0.05}$ (1)	$-3.49^{+0.05}_{-0.05}$	0.46 ± 0.04
J133031.75-003611.9 (S)	0.0542	23	4.2	4.4	85.8 ± 12.2	<41.02 (0)	< −3.64	0.60 ± 0.03
J133032.00-003613.5 (P)	0.0542	23	4.2	4.4	142.0 ± 10.6	$40.96^{+0.15}_{-0.19}$ (1)	$-4.62^{+0.15}_{-0.19}$	0.60 ± 0.03
J154403.45+044607.5 (S)	0.0420	113	4.1	3.4	124.4 ± 13.4	<40.78 (1)	< −4.56	−0.11 ± 0.23
J154403.67+044610.1 (P)	0.0416	113	4.1	3.4	200.2 ± 8.7	$41.55^{+0.06}_{-0.07}$ (1)	$-4.67^{+0.06}_{-0.07}$	-0.11 ± 0.23
J220634.97+000327.6 (S)	0.0466	130	4.7	4.3	74.8 ± 9.0	<40.86 (0)	< −3.54	0.14 ± 0.03
J220635.08+000323.2 (P)	0.0461	130	4.7	4.3	172.9 ± 8.6	$41.75^{+0.05}_{-0.06}$ (1)	$-4.19^{+0.05}_{-0.06}$	0.14 ± 0.03

Note. (1) SDSS names with J2000 coordinates given in the form of "hhmmss.ss+ddmmss.s"; the targets are listed in the order of RA; "P" and "S" denote the primary and secondary nuclei according to the stellar velocity dispersion; (2) spectroscopic redshift from the SDSS DR7, based on the fit to the stellar continuum; (3) velocity offset of the two nuclei in each pair, in units of km s^{-1}; (4)–(5) projected angular and physical separation of the two nuclei in each pair, in units of arcsecond and kiloparsec, respectively; (6) stellar velocity dispersion, in units of km s^{-1}, derived with pPXF (Cappellari & Emsellem 2004); (7) absorption corrected luminosities of the nucleus in the 2–10 keV band with a presumed absorption column density of 10^{22} cm^{-2} and a power-law photon index of 1.7, in units of erg s^{-1}, from H20; 1 and 0 in parentheses represent detection and nondetection in X-rays in the 0.5–8 keV band, respectively; (8) X-ray Eddington ratio; (9) WISE W1(3.4 μm)–W2(4.6 μm) color, from Wright et al. (2010), in units of magnitude.

higher angular resolution of $\sim 0\farcs9$, which corresponds to a typical linear scale of 1 kpc at the distance of our targets and is sufficient to distinguish the two nuclei. The exposure time for each target ranged from 0.4 to 4.5 hr. We used the PolyFiX correlator in Band 3. The tuning frequency was set according to the mean redshift of each target pair. The flux calibrators included LKHA101, MWC349, and 1055+018, which have a systematic uncertainty of $\lesssim$20%.

The data reduction and calibration were performed using the CLIC package of GILDAS (versions oct21a)[9] following the standard procedure. The image cleaning and analysis were done with the MAPPING package of GILDAS. We binned the frequency channels by a factor of 5 to achieve an effective velocity resolution of $\sim$14 km s^{-1}, which is optimal for the signal-to-noise ratio (S/N) of the line emission given the expected velocity dispersion of the circumnuclear gas. We adopted the natural weighting, HOGBOM algorithm, and cleaned the image down to the one time of the noise level determined by the initial clean version of the image with the central source region masked. Basic information of the CO observations are reported in Table 2.

3. Detection of Circumnuclear Molecular Gas

3.1. Molecular Gas Measurement

We exported the data to a CASA-compatible format and performed CO measurement in CASA (version 6.3.0.48, McMullin et al. 2007). We removed all the pixels in the data cube with S/N less than 3 and created moment maps for each target using the *immoments* task. We further used the Source Finding Application (SoFiA, Serra et al. 2015) to highlight the source region and generated a new version of the maps for better visualization. The resultant line intensity (moment zero), velocity (moment one), and velocity dispersion (moment two) maps are shown in Figure 1; 10 of the 14 nuclei have a clear detection of CO(2–1) emission. Specifically, four dual-AGN systems (J1027+1749, J1058+3114, J1544+0446, and J2206+0003) have both nuclei detected, two systems (J0858+1822 and J1330−0036) have only one nucleus detected, and the remaining system (J0022+0022) has no CO detection in either nucleus, which is not shown in Figure 1. The CO emission of most detected nuclei are spatially compact. Figure 2 shows the CO(2–1) line profiles of the detected nuclei, which are constructed by summing up pixels above three times the rms level in the moment zero map. Below we provide brief remarks on the individual pairs, and we defer a detailed study of the gas spatial distribution and kinematics to a future work.

For J0858+1822, molecular gas is only detected in the primary nucleus, but there is an appreciable offset ($\sim 2''$) between the optical position of the primary nucleus and the peak of CO emission in the intensity map. The peak of the velocity dispersion map is also significantly offset from the optical nucleus. The velocity field appears to be dominated by a rotating structure (i.e., the redshifted and blueshifted components are roughly symmetrical), but the line profile exhibits an excess on the redshifted (positive) side up to $\sim$400 km s^{-1} from the velocity peak. Such noncircular motions might be due to an infalling stream or an outflow of molecular gas. No clear excess can be associated with the secondary nucleus, although this might be partially owing to the close separation between the two nuclei. Overall these features suggest a merger system in the late stage, where the molecular gas in the individual galaxies are being mixed but not yet fully settled. For J1027+1749, molecular gas is detected in both nuclei but is more concentrated around the secondary nucleus. The velocity field around each nucleus is consistent with a rotating structure (e.g., a disk or a tori) but also shows faint noncircular features, which are also evident in the line profile. For J1058+3114, which has the best angular resolution among all pairs, molecular gas is detected in both nuclei. Additionally, there is a clump of

[9] https://www.iram.fr/IRAMFR/GILDAS

Table 2
NOEMA CO Observations of Seven Dual AGNs

Name (1)	Date (2)	Exp (3)	Freq (4)	Beam Size (5)	PA (6)	V_{mean} (7)	$S_{CO}\Delta V$ (8)	N_H (9)	M_{H_2} (10)
J0022+0022S	2020-10-24	0.4	215.3	1.43 × 0.71	5.4	⋯	<0.88	<0.27	<0.23
J0022+0022P	2020-10-24	0.4	215.3	1.43 × 0.71	5.4	⋯	<0.81	<0.25	<0.21
J0858+1822S	2020-11-1	0.6	217.7	3.63 × 1.38	169.1	⋯	<1.44	<0.09	<0.26
J0858+1822P	2020-11-1	0.6	217.7	3.63 × 1.38	169.1	118.9	74.30 ± 1.20	4.64 ± 0.07	13.25 ± 0.21
J1027+1749P	2020-11-23	0.9	216.1	4.61 × 0.95	4.2	81.2	18.23 ± 0.98	1.29 ± 0.07	4.15 ± 0.22
J1027+1749S	2020-11-23	0.9	216.1	4.61 × 0.95	4.2	−59.9	90.60 ± 1.50	6.49 ± 0.11	20.68 ± 0.34
J1058+3144S	2020-11-5	1.1	214.9	1.07 × 0.75	40.6	5.2	2.18 ± 0.08	1.03 ± 0.04	0.60 ± 0.02
J1058+3144P	2020-11-5	1.1	214.9	1.07 × 0.75	40.6	−48.3	5.83 ± 0.08	2.97 ± 0.04	1.58 ± 0.02
J1330-0036S	2020-11-22	2.6	218.7	2.29 × 0.80	8.4	⋯	<0.45	<0.08	<0.07
J1330-0036P	2020-11-22	2.6	218.7	2.29 × 0.80	8.4	26.3	25.61 ± 0.19	17.84 ± 0.13	3.85 ± 0.03
J1544+0446S	2021-1-6	1.0	221.2	3.51 × 0.89	8.1	−70.6	34.30 ± 0.34	3.49 ± 0.03	3.07 ± 0.03
J1544+0446P	2021-1-6	1.0	221.2	3.51 × 0.89	8.1	−34.6	40.80 ± 0.55	12.62 ± 0.17	3.59 ± 0.05
J2206+0003S	2020-10-24	0.3	220.3	1.52 × 0.94	0.0	0.7	4.11 ± 0.03	0.91 ± 0.01	0.46 ± 0.01
J2206+0003P	2020-10-24	0.3	220.3	1.52 × 0.94	0.0	−83.8	2.06 ± 0.03	0.46 ± 0.01	0.22 ± 0.01

Note. (1) Abbreviated names. 'P' and 'S' denote the primary and secondary nuclei according to the stellar velocity dispersion; (2) observation date; (3) effective on-source time based on visibilities after flagging data in units of hours; (4) observed frequency in units of GHz; (5) synthesized beam size in units of $'' \times ''$; (6) position angle of the synthesized beam in units of degrees; (7) intensity-weighted mean velocity, relative to the tuning frequency in units of km s^{-1}; (8) NOEMA CO(2–1) 230 GHz flux density in units of Jy km s^{-1}; for nondetected nuclei, 3σ upper limits are given; (9) hydrogen column density converted from CO(2–1) in units of 10^{22} cm^{-2}; (10) derived molecular hydrogen mass in units of $10^9\,M_\odot$.

molecular gas in the north of the primary nucleus, which is spatially coincident with the northern spiral arm of the primary galaxy and has a velocity offset (∼300 km s^{-1}) from the two nuclei. The velocity field around the primary nucleus is consistent with a resolved rotating structure, but the rather flat-topped line profile suggests that molecular gas is not centrally concentrated. The secondary nucleus is rather compact, but also exhibits small deviations from an otherwise narrow and symmetric line profile. For J1330−0036, molecular gas is only detected in the primary nucleus. Both the morphology and line profile suggest the presence of extended features in addition to the bright compact core, which are mostly seen between the two nuclei. This may indicate an ongoing mixing of gas from the two galaxies. A faint patch of CO emission can also be seen around the secondary nucleus in the intensity map, but it is possibly contaminated by an interference fringe; thus we conservatively treat it as a nondetection. For J1544+0446, molecular gas is detected in both nuclei. The primary nucleus exhibits a double-peaked line profile, which is reminiscent of a centrally depleted rotating disk or a ring. The FWHM of the line reaches ∼600 km $^{-1}$, the highest among all detected nuclei. Moreover, the peak of velocity dispersion is offset from the optical nucleus and reaches ∼230 km s^{-1}, also the highest value seen among all nuclei, which may indicate the presence of tidal shocks or an outflow. The secondary nucleus shows a centrally peaked and symmetric profile. For J2206+0003, molecular gas is detected in both nuclei, which appear well separated from each other. The velocity field of both nuclei indicates a compact rotating structure, and the flat-topped line profile seen in the secondary nucleus suggests that this structure is centrally depleted.

We quantify the CO(21) emission from each nucleus using the CASA task *IMFIT*. On the intensity map, each nucleus is fitted by a two-dimensional Gaussian model, which is a good approximation for the observed CO intensity distribution. The CO(21) luminosity is then calculated following Solomon & Vanden Bout (2005)

$$L'_{CO} = 3.25 \times 10^7\, S_{CO}\,\Delta V\,\nu_{obs}^{-2}\,D_L^2\,(1+z)^{-3}, \quad (1)$$

where L'_{CO} is the CO line luminosity in units of K km s^{-1} pc^2, $S_{CO}\Delta V$ is the CO integrated flux density in units of Jy km s^{-1}, ν_{obs} is the observed frequency in GHz, and D_L is the luminosity distance in Mpc. For the nondetected nuclei, we estimate a 3σ upper limit of $S_{CO}\Delta V$ by $3\sigma_{ch}(\Delta V_{ch} \times \Delta V_{line})^{1/2}$ (Seaquist et al. 1995; Wagg et al. 2007), where the σ_{ch} and ΔV_{ch} are the channel rms and width, respectively, ΔV_{line} is the line-of-sight velocity range of the CO line, assuming the same value of the neighboring detected nucleus (for the case of J0022+0022, where both nuclei are nondetected, $\Delta V_{line} = 500$ km s^{-1} is assumed). To derive the equivalent hydrogen column density (N_H) and the molecular hydrogen mass (M_{H_2}), we adopt the conventional CO-to-H_2 conversion factor $X_{CO} = 2 \times 10^{20}$ cm^{-2} (K km s^{-1})$^{-1}$ and $\alpha_{CO} = 4.3\,M_\odot$ (K km s^{-1} pc^2)$^{-1}$, which are suitable for the CO(10) line (Bolatto et al. 2013). To further convert into CO(2–1), we have assumed an intrinsic CO(2–1)/CO(1–0) intensity ratio $R_{21} = 1$, which is not atypical for galactic nuclei (e.g., Leroy et al. 2009; Li et al. 2019). The hence derived beam-averaged CO-based column density, $N_H = X_{CO} \times R_{21} \times L'_{CO}/\Omega$, ranges from 4.6×10^{21} to 1.79×10^{23} cm^{-2} for the 10 detected nuclei (Table 2). Here Ω is the area of the synthesized beam. We note that the actual column density could be higher if the detected CO emission arises from a region significantly smaller than the beam (see further discussions in Section 4). For the four nondetected nuclei, the 3σ upper limits of N_H are similarly converted from the upper limit of L'_{CO}, which ranges from 0.8×10^{21} to 2.7×10^{21} cm^{-2}. The corresponding values of M_{H_2}, ranging between $(0.07–20.75) \times 10^9\ M_\odot$, are also listed in Table 2. We note that the uncertainty related to X_{CO} and R_{21}, which should not exceed a factor of a few, does not affect the main conclusion drawn below.

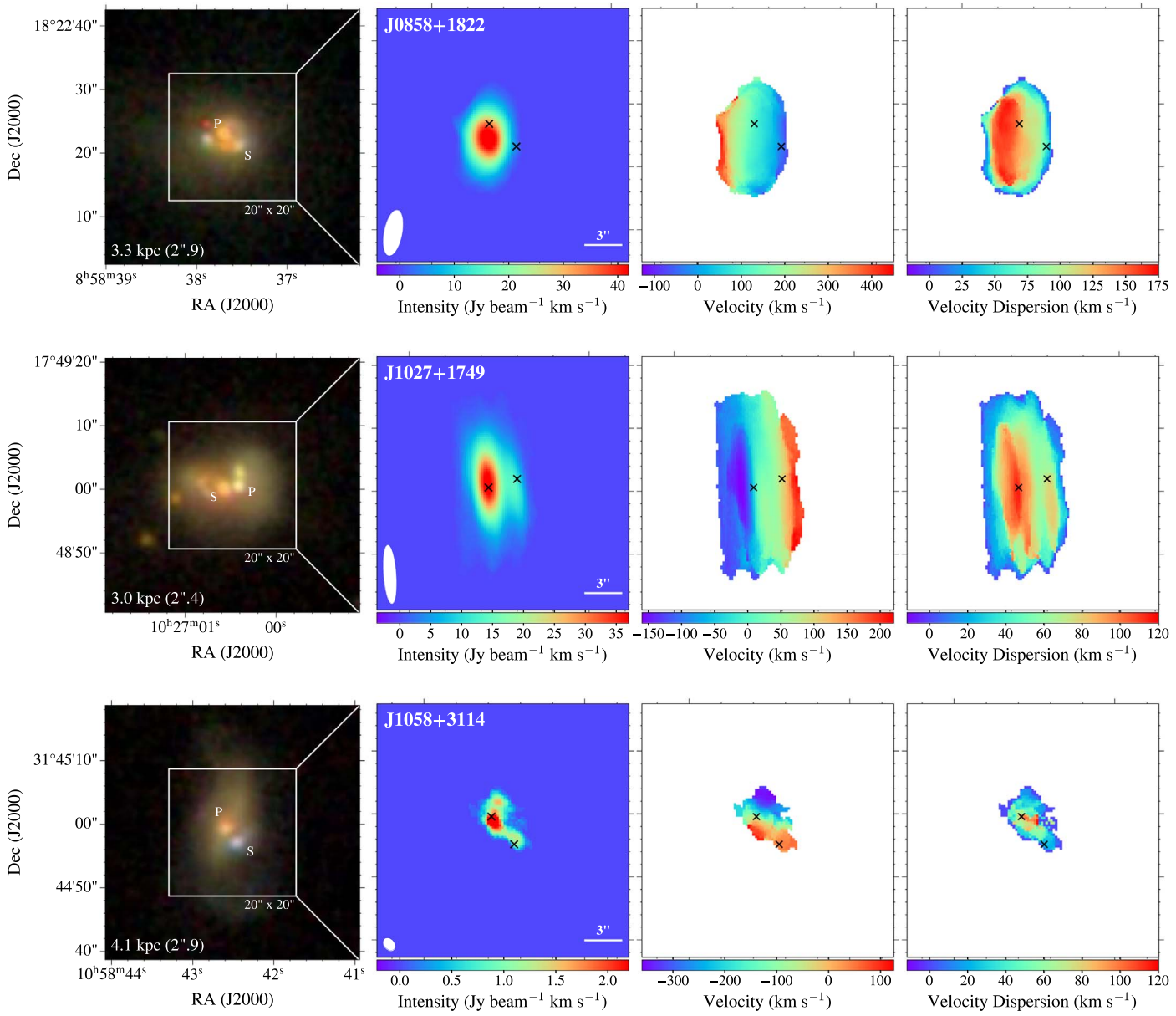

Figure 1. Six dual-AGN systems with at least one nucleus detected in CO(2–1) emission. The SDSS *gri*-color composite image is shown in the left panel, and the NOEMA CO(2–1) moment zero, one, and two maps (intensity, velocity, and velocity dispersion maps) are shown in the right three panels with a size of 20″ × 20″. North is up and east is to the left. The pairs are ordered in increasing R.A. For each pair, the projected physical separation is labeled with angular distance in parenthesis. "P" and "S" denote the primary and secondary nuclei according to the stellar velocity dispersion. Crosses in the moment maps mark positions of the optical nuclei. The synthesized beam is showed in the lower-left corner of the moment zero map.

3.2. Correlations with X-Ray and Optical Properties

One of the primary goals of this work is to understand whether the apparently low X-ray luminosities of the dual AGNs are due to strong circumnuclear obscuration. Figure 3 displays the equivalent hydrogen column density derived from the CO(2–1) emission versus the 2–10 keV X-ray luminosity (L_X, left panel) and the X-ray Eddington ratio ($f_{Edd,X} = L_X/L_{Edd}$, right panel) for each nucleus in our sample. The Eddington ratio is defined as L_X normalized by the Eddington luminosity (L_{Edd}) of the given nucleus, originally calculated by H20 according to the black hole mass–stellar velocity dispersion relation and here updated for the revised stellar velocity dispersion. The 14 nuclei have very moderate $L_X \lesssim 2 \times 10^{42}$ erg s^{-1} and highly sub-Eddington $f_{Edd,X} \lesssim 3 \times 10^{-4}$. We note that the X-ray luminosity, or its upper limit, was primarily estimated by assuming a canonical spectral model, i.e., an absorbed power law with a presumed absorption column density $N_{H,X} = 10^{22}$ cm^{-2} and a photon dex of 1.7 (H20). Such a treatment was appropriate for the limited number of X-ray counts for most nuclei, but could have significantly underestimated the intrinsic absorption column density.

Nevertheless, it can be seen from Figure 3 that the CO-based N_H has typical values of $\sim 10^{22}$ cm^{-2} and in all cases below $\sim 2 \times 10^{23}$ cm^{-2}. Moreover, four of the hard X-ray-undetected nuclei, J0022+0022S, J0022+0022P, J0858+1822S, and J1330-0036S, are also undetected in CO(2–1), and the two nuclei with the highest L_X, J1058+3144P and J2206+0003S, have only a moderate CO-based N_H. In the two nuclei with $N_H \sim (1-2) \times 10^{23}$cm^{-2}, there might be substantial intrinsic X-ray obscuration, but raising

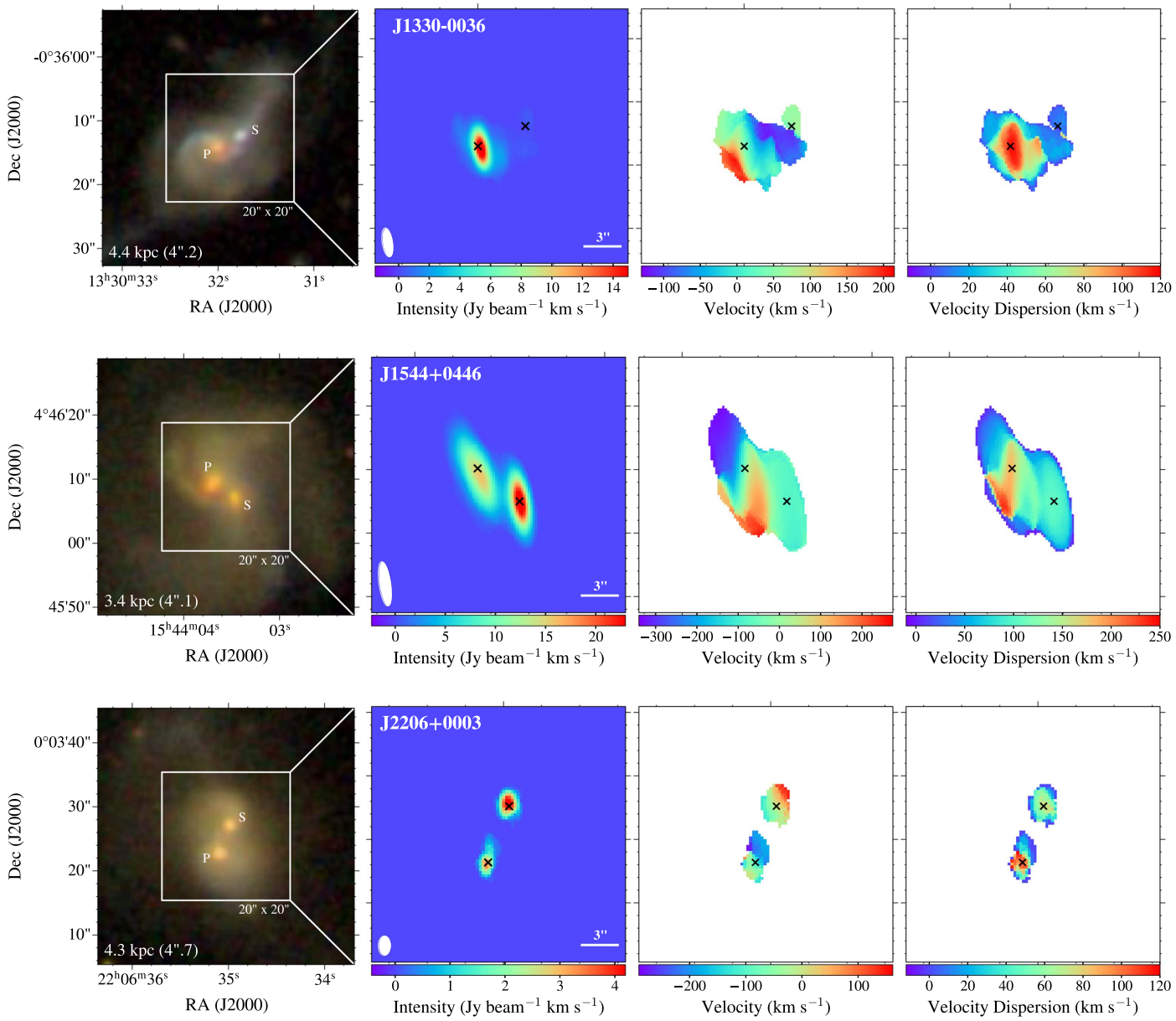

Figure 1. (Continued.)

the assumed $N_{\rm H,X}$ from 10^{22} to 10^{23} cm^{-2} would lead to an increase of $L_{\rm X}$ and $f_{\rm Edd,X}$ by only a factor of $\sim$2. Overall, the amount of circumnuclear molecular gas is moderate in the present sample of dual AGNs, which argues against strong X-ray obscuration being prevalent in these systems (see further discussions in Section 4).

Lastly, we note the interesting trend that in four pairs the higher $N_{\rm H}$ and $M_{\rm H_2}$ are found with the primary nucleus (marked by solid symbols in Figure 3). The exceptions are J1027+1749 and J2206+0003, in which the secondary has an $N_{\rm H}$ about 5 and 2 times higher than that of the primary, respectively. The remaining pair, J0022+0022, has no significant CO detected in either host galaxy. Such a trend, if further supported by a larger sample of close pairs, might be understood as the more massive nucleus/host galaxy being more likely to accumulate a substantial amount of cold gas due to a stronger gravitational potential.

4. Summary and Discussion

Utilizing NOEMA CO(2–1) observations, we have conducted a pilot survey of circumnuclear molecular gas in seven dual-AGN systems at a redshift $\sim$0.06. These systems have the smallest projected separation ($r_{\rm p} \lesssim 5$ kpc) among the optically and X-ray selected AGN pairs studied by H20, providing an important close-up view of AGN activity at or close to the late stage of galaxy mergers. The high-resolution NOEMA observations are able to resolve the two closely separated nuclei in a pair. Significant CO(2–1) emission is detected in 10 of the 14 nuclei, which traces circumnuclear molecular gas with a sensitivity equivalent to a limiting hydrogen column density of $\sim 1.0 \times 10^{21}$ cm^{-2}, assuming a standard CO-to-H_2 conversion factor and a CO(2–1)/CO(1–0) intensity ratio of unity. The derived equivalent hydrogen column density ranges between 5×10^{21} and 2×10^{23} cm^{-2}, but mostly at values of a few times 10^{22} cm^{-2}. Most CO-detected nuclei show a

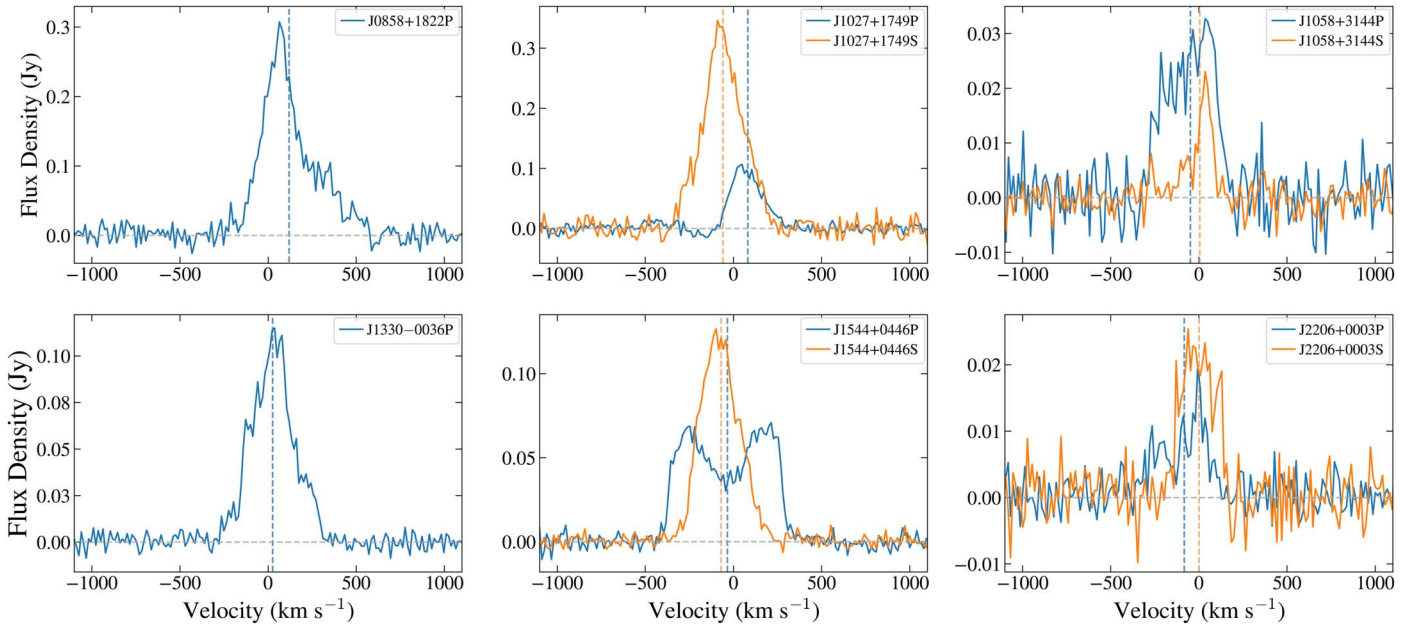

Figure 2. CO(2–1) line profile of the detected nuclei, blue for the primary and orange for the secondary (when detected). The vertical dashed lines mark the intensity-weighted mean velocity.

compact morphology, but extended CO emission is also found in at least two cases (J1058+3144P and J2206+0003S). The CO velocity field and line profile of most nuclei are consistent with a rotating structure, but noncircular motions are also evident in some cases.

H20 found that all 14 nuclei have a moderate 2–10 keV luminosity $\lesssim 2\times10^{42}\,\mathrm{erg\,s^{-1}}$ and a low Eddington ratio $\lesssim 3\times10^{-4}$ (Figure 3). This is rather surprising, as galaxy pairs at such small projected separations ($\lesssim$5 kpc) are expected to have experienced strong gravitational torques, which induce gas inflows to the galactic nucleus and subsequently trigger active SMBH accretion. This has been extensively demonstrated by numerical simulations of idealized galaxy mergers (e.g., Capelo et al. 2015; Capelo & Dotti 2017; Solanes et al. 2019; Yang et al. 2019), although until recently numerical simulations still rely on prescriptions of subgrid physics to account for accretion, radiation, and feedback of the SMBH (De Rosa et al. 2019). One possibility to reconcile the apparently low X-ray luminosities is strong absorption typical of Compton-thick AGNs, which have a line-of-sight column density $N_{\rm CT}\gtrsim10^{24}\,\mathrm{cm^{-2}}$, such that X-ray photons with an energy below a few keV are completely obscured. However, none of the 14 nuclei show a CO-based hydrogen column density above the Compton-thick threshold, and in fact, the majority fall bellow $10^{23}\,\mathrm{cm^{-2}}$. A potential caveat is that this $N_{\rm H}$ is derived by averaging over the synthesized beam of the NOEMA observation, which corresponds to a physical scale of $\lesssim$few kpc, whereas direct absorption of the X-rays may arise from a smaller (10–100 pc) region around the SMBH. If the detected CO emission arises from this more compact region, the actual column density could be much greater. For instance, a recent study by García-Burillo et al. (2021) based on high-resolution Atacama Large Millimeter/submillimeter Array (ALMA) survey of nearby Seyfert galaxies detected spatially resolved dusty molecular tori located around the AGN, which have a median torus diameter of ∼42 pc. The molecular gas column density, $N(\mathrm{H_2})$, derived from the CO emission, shows a typical range ($\sim8\times10^{21}$–$4\times10^{23}\,\mathrm{cm^{-2}}$) similar to our sample, but for five low-luminosity AGNs in their sample ($L_{2-10\,\mathrm{keV}}\sim10^{40}\,\mathrm{erg\,s^{-1}}$), the molecular gas column densities are much higher ($\sim10^{24}\,\mathrm{cm^{-2}}$).

However, such a case is unlikely to be relevant to the majority of our sample, for the following considerations. First, among the whole sample, the three systems (J0022+0022, J1058+3144, and J2206+0003) with the best physical resolution (∼1.5–2 kpc) are also among the ones with the lowest CO-based $N_{\rm H}$ (perhaps except for J1058+3144P). Second, among the whole sample, three nuclei have a sufficient number of detected X-ray counts for a spectral analysis. Following Hou et al. (2019), we adopt an absorbed power-law model to fit the spectra of these nuclei. The best-fit absorption column density ($N_{\rm H,X}$) is found to be $6.4^{+6.3}_{-4.5}\times10^{22}\,\mathrm{cm^{-2}}$, $3.9^{+3.2}_{-2.7}\times10^{22}\,\mathrm{cm^{-2}}$, and $5.7^{+23.7}_{-3.7}\times10^{22}\,\mathrm{cm^{-2}}$, for J1058+3144P, J1544+0446P, and J2206+0003S, respectively. These values are consistent with the CO-based $N_{\rm H}$ within a factor of ∼2, indicating that the latter is a good proxy to the actual absorption column density. In fact, the CO-based column density and X-ray-based column density are also consistent within a factor of ∼2 in the Seyfert galaxies studied by (García-Burillo et al. 2021, Figure 17 therein). Third, the infrared color can provide an independent probe of luminous AGNs ($L_{\rm X}\gtrsim10^{43}\,\mathrm{erg\,s^{-1}}$; Jarrett et al. 2011; Stern et al. 2012), in the standard picture in which a dusty torus absorbs the central engine's intense X-ray/ultraviolet radiation and subsequently reradiates copious infrared emission. Specifically, a Wide-field Infrared Survey Explorer (WISE; Wright et al. 2010) color cut, W1(3.4 μm)–W2(4.6 μm) >0.8, robustly separates luminous AGNs from star-forming galaxies (Stern et al. 2012). It turns out all seven dual AGNs studied here have W1−W2 < 0.8 (Table 1), with a median value of 0.2. Even with the more conservative cut of W1 −W2 > 0.5 suggested by Satyapal et al. (2014; see also discussions by Blecha et al. 2018), which tolerates weaker AGNs, only one system (J1330−0036) satisfies the threshold with its W1 − W2 ≈ 0.6. This suggests that no intrinsically luminous AGN exists in the majority, if not all, of the seven systems. We note that given the relatively large

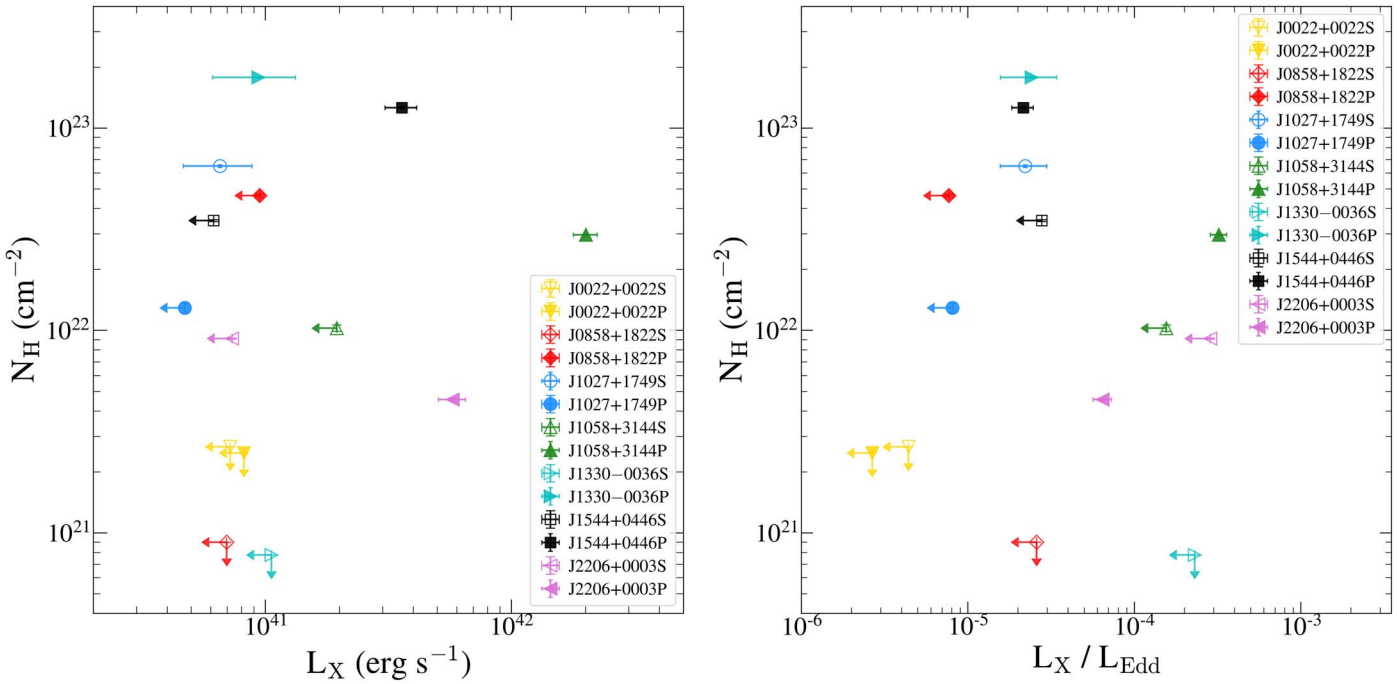

Figure 3. Beam-averaged CO-based equivalent hydrogen column density versus 2–10 keV X-ray luminosity (left panel) and X-ray Eddington ratio (right panel) for the 14 nuclei in seven pairs of dual AGNs; 3σ upper limits of the nondetected (in CO or X-rays) nuclei are denoted by arrows. The primary and secondary nuclei are marked by solid and open symbols, respectively.

WISE point-spread function (FWHM $\sim 6''$), the two nuclei in any of the seven pairs are unresolved and thus share the same value. Nevertheless, this should not alter the above conclusion.

Therefore, we conclude that the moderate X-ray luminosities found in the seven dual AGNs are unlikely due to circumnuclear obscuration, but should reflect the prevalence of weakly accreting SMBHs in these nuclei. This may seem surprising for these merging systems at or close to their late evolutionary stage. H20 proposed a plausible explanation that involves a feeding-and-feedback loop, which we elaborate on here. In this picture, AGN activity is triggered in one or both of the SMBHs by the pericentric passage of the two host galaxies. The subsequent AGN feedback can halt the gas inflow, expel gas from the central region, and suppress subsequent SMBH accretion. This feedback is likely in a kinetic mode, given that the accretion rates inferred from the X-ray luminosities of the dual AGNs are generally highly sub-Eddington (Figure 3; H20). Recently, Peng et al. (2022) reported clear evidence of ongoing AGN feedback in the candidate triple-AGN system, SDSS J0849+1114, in which kiloparsec-scale, energetic radio jets are present in two of the three optical nuclei. The estimated jet energetics (a few 10^{55} erg) are comparable to that needed to unbind a cold gas of $\sim 10^8\,M_\odot$ from the central $\sim$100 pc of the host galaxy. Thus, this fine example is quite relevant to the feedback scenario discussed here. Alternatively, the AGN feedback might be predominantly radiative, which pushes out the dusty gas via radiative pressure (e.g., Ricci et al. 2022). However, for the radiative mode to be dominant, the accretion rate should be close to the Eddington limit, which must be rare given the statistical result of H20.

Two potential issues with the AGN feedback scenario deserve further remarks. First, not *all* 14 nuclei are deficient in circumnuclear molecular gas. Indeed two nuclei (J0858+1822P and J1027+1749S) have $\sim 10^{10}\,M_\odot$ of gas detected within the central few kiloparsecs, which is comparable to gas-rich normal galaxies. On the other hand, at least three nuclei (J1058+3144P, J1544+0446S, J2206+0003S) show a flat-topped line profile, which suggests that the gas is not centrally concentrated, consistent with depletion of gas in the close vicinity of the SMBH. Higher-resolution CO observations, e.g., possibly afforded by ALMA, would be helpful to confirm a paucity of cold gas within the gravitational influence radius ($\lesssim$100 pc) of the SMBHs in these nuclei. Second, for the feedback scenario to be compatible with the low luminosities and low accretion of essentially all nuclei studied here, it would require a relatively short phase of active accretion and strong feedback. This is most feasible with the second pericentric passage of the merging pair, which simulations predict to boost AGN activity for a few tens of Myr when the two nuclei are separated by a few kiloparsecs (e.g., Capelo et al. 2015). After that, the accretion rate drops back to and maintains at a low level until the two galaxies finally merge. High-resolution radio and optical spectroscopic observations are warranted to search for direct evidence of AGN feedback in these and other kiloparsec-scale dual AGNs, especially the ones with relatively high Eddington ratios.

This work is based on observations carried out under project number S20BJ with the IRAM NOEMA Interferometer. IRAM is supported by INSU/CNRS (France), MPG (Germany), and IGN (Spain). Special acknowledgment is dedicated to the late Dr. Yu Gao, whose encouragement made this NOEMA program possible. M.H. wishes to thank Vinod Arumugam for his assistance with the NOEMA observation and data reduction, Yanmei Chen, Y. Sophia Dai, Fengyuan Liu, and Zhiyu Zhang for helpful discussions. M.H. is supported by the National Natural Science Foundation of China (12203001) and the fellowship of China National Postdoctoral Program for Innovation Talents (grant BX2021016). L.C.H. was supported by the National Science Foundation of China (11721303,

11991052, 12011540375) and the China Manned Space Project (CMS-CSST-2021-A04, CMS-CSST-2021-A06). Z.L. acknowledges support by the National Key Research and Development Program of China (2017YFA0402703) and National Natural Science Foundation of China (11873028). X.L. acknowledges support from NSF grants AST-2108162 and AST-2206499.

ORCID iDs

Meicun Hou https://orcid.org/0000-0001-9062-8309
Zhiyuan Li https://orcid.org/0000-0003-0355-6437
Xin Liu https://orcid.org/0000-0003-0049-5210
Zongnan Li https://orcid.org/0000-0002-7172-6306
Ruancun Li https://orcid.org/0000-0001-8496-4162
Ran Wang https://orcid.org/0000-0003-4956-5742
Jing Wang https://orcid.org/0000-0002-6593-8820
Luis C. Ho https://orcid.org/0000-0001-6947-5846

References

Barnes, J. E., & Hernquist, L. 1992, ARA&A, 30, 705
Barton, E. J., Geller, M. J., & Kenyon, S. J. 2000, ApJ, 530, 660
Blecha, L., Snyder, G. F., Satyapal, S., & Ellison, S. L. 2018, MNRAS, 478, 3056
Bolatto, A. D., Wolfire, M., & Leroy, A. K. 2013, ARA&A, 51, 207
Brightman, M., Balokovic, M., Koss, M., et al. 2018, ApJ, 867, 110
Capelo, P. R., & Dotti, M. 2017, MNRAS, 465, 2643
Capelo, P. R., Volonteri, M., Dotti, M., et al. 2015, MNRAS, 447, 2123
Cappellari, M., & Emsellem, E. 2004, PASP, 116, 138
Comerford, J. M., Gerke, B. F., Newman, J. A., et al. 2009, ApJ, 698, 956
Comerford, J. M., Pooley, D., Gerke, B. F., & Madejski, G. M. 2011, ApJL, 737, L19
Darg, D. W., Kaviraj, S., Lintott, C. J., et al. 2010, MNRAS, 401, 1043
De Rosa, A., Vignali, C., Bogdanovic, T., et al. 2019, NewAR, 86, 101525
De Rosa, A., Vignali, C., Husemann, B., et al. 2018, MNRAS, 480, 1639
Di Matteo, T., Springel, V., & Hernquist, L. 2005, Natur, 433, 604
Ellison, S. L., Patton, D. R., Mendel, J. T., & Scudder, J. M. 2011, MNRAS, 418, 2043
Ellison, S. L., Patton, D. R., Simard, L., & McConnachie, A. W. 2008, AJ, 135, 1877
Ellison, S. L., Secrest, N. J., Mendel, J. T., Satyapal, S., & Simard, L. 2017, MNRAS, 470, L49
Evans, A. S., Mazzarella, J. M., Surace, J. A., & Sanders, D. B. 2002, ApJ, 580, 749
Feruglio, C., Fiore, F., Carniani, S., et al. 2015, A&A, 583, A99
Fu, H., Myers, A. D., Djorgovski, S. G., et al. 2015a, ApJ, 799, 72
Fu, H., Wrobel, J. M., Myers, A. D., Djorgovski, S. G., & Yan, L. 2015b, ApJL, 815, L6
Gabanyi, K. É, An, T., Frey, S., et al. 2016, ApJ, 826, 106
García-Burillo, S., Alonso-Herrero, A., Ramos Almeida, C., et al. 2021, A&A, 652, A98
Ge, J.-Q., Hu, C., Wang, J.-M., Bai, J.-M., & Zhang, S. 2012, ApJS, 201, 31
Goulding, A. D., Greene, J. E., Bezanson, R., et al. 2018, PASJ, 70, S37
Herrera-Camus, R., Janssen, A., Sturm, E., et al. 2020, A&A, 635, A47
Ho, L. C. 2008, ARA&A, 46, 475
Ho, L. C. 2009, ApJ, 699, 626
Hopkins, P. F., Kocevski, D. D., & Bundy, K. 2014, MNRAS, 445, 823
Hou, M., Li, Z., & Liu, X. 2020, ApJ, 900, 79
Hou, M., Liu, X., Guo, H., et al. 2019, ApJ, 882, 41
Jarrett, T. H., Cohen, M., Masci, F., et al. 2011, ApJ, 735, 112
Kaneko, H., Kuno, N., Iono, D., et al. 2013, PASJ, 65, 20
Kaneko, H., Kuno, N., Iono, D., et al. 2017, PASJ, 69, 66
Kauffmann, G., & Haehnelt, M. 2000, MNRAS, 311, 576
Kewley, L. J., Geller, M. J., & Barton, E. J. 2006, AJ, 131, 2004
Koss, M., Mushotzky, R., Treister, E., et al. 2012, ApJL, 746, L22
Koss, M., Mushotzky, R., Veilleux, S., & Winter, L. 2010, ApJL, 716, L125
Leroy, A. K., Walter, F., Bigiel, F., et al. 2009, AJ, 137, 4670
Li, Z., Li, Z., Zhou, P., et al. 2019, MNRAS, 484, 964
Liu, X., Civano, F., Shen, Y., et al. 2013, ApJ, 762, 110
Liu, X., Shen, Y., & Strauss, M. A. 2012, ApJ, 745, 94
Liu, X., Shen, Y., Strauss, M. A., & Greene, J. E. 2010, ApJ, 708, 427
Liu, X., Shen, Y., Strauss, M. A., & Hao, L. 2011, ApJ, 737, 101
Lyu, Y., & Liu, X. 2016, MNRAS, 463, 24
McMullin, J. P., Waters, B., Schiebel, D., Young, W., & Golap, K. 2007, in ASP Conf. Ser. 376, Astronomical Data Analysis Software and Systems XVI, ed. R. A. Shaw, F. Hill, & D. J. Bell (San Francisco, CA: ASP), 127
Menci, N., Gatti, M., Fiore, F., & Lamastra, A. 2014, A&A, 569, A37
Michiyama, T., Iono, D., Nakanishi, K., et al. 2016, PASJ, 68, 96
Nikolic, B., Cullen, H., & Alexander, P. 2004, MNRAS, 355, 874
Olson, K. M., & Kwan, J. 1990, ApJ, 349, 480
Peng, S., Li, Z., Liu, X., et al. 2022, ApJ, 934, 89
Ricci, C., Ananna, T. T., Temple, M. J., et al. 2022, ApJ, 938, 67
Sakamoto, K., Aalto, S., Combes, F., Evans, A., & Peck, A. 2014, ApJ, 797, 90
Sakamoto, K., Wang, J., Wiedner, M. C., et al. 2008, ApJ, 684, 957
Satyapal, S., Ellison, S. L., McAlpine, W., et al. 2014, MNRAS, 441, 1297
Satyapal, S., Secrest, N. J., Ricci, C., et al. 2017, ApJ, 848, 126
Seaquist, E. R., Ivison, R. J., & Hall, P. J. 1995, MNRAS, 276, 867
Serra, P., Westmeier, T., Giese, N., et al. 2015, MNRAS, 448, 1922
Shangguan, J., Ho, L. C., Li, R., et al. 2019, ApJ, 870, 104
Silverman, J. D., Kampczyk, P., Jahnke, K., et al. 2011, ApJ, 743, 2
Sliwa, K., Wilson, C. D., Matsushita, S., et al. 2017, ApJ, 840, 8
Smith, K. L., Shields, G. A., Bonning, E. W., et al. 2010, ApJ, 716, 866
Solanes, J. M., Perea, J. D., Valentí-Rojas, G., et al. 2019, A&A, 624, A86
Solomon, P. M., & Vanden Bout, P. A. 2005, ARA&A, 43, 677
Stern, D., Assef, R. J., Benford, D. J., et al. 2012, ApJ, 753, 30
Tan, Q.-H., Gao, Y., Daddi, E., et al. 2021, ApJ, 913, 82
Teng, S. H., Schawinski, K., Urry, C. M., et al. 2012, ApJ, 753, 165
Thorp, M. D., Ellison, S. L., Pan, H.-A., et al. 2022, MNRAS, 516, 1462
Toomre, A., & Toomre, J. 1972, ApJ, 178, 623
Villforth, C., Hamann, F., Rosario, D. J., et al. 2014, MNRAS, 439, 3342
Villforth, C., Hamilton, T., Pawlik, M. M., et al. 2017, MNRAS, 466, 812
Violino, G., Ellison, S. L., Sargent, M., et al. 2018, MNRAS, 476, 2591
Wagg, J., Hughes, D. H., Aretxaga, I., et al. 2007, MNRAS, 375, 745
Weston, M. E., McIntosh, D. H., Brodwin, M., et al. 2017, MNRAS, 464, 3882
Wright, E. L., Eisenhardt, P. R. M., Mainzer, A. K., et al. 2010, AJ, 140, 1868
Yang, C., Ge, J.-Q., & Lu, Y.-J. 2019, RAA, 19, 177